Christopher Katinas
School of Mechanical Engineering,
Purdue University,
West Lafayette, IN 47907
e-mail: ckatinas@purdue.edu

Weixiao Shang
School of Mechanical Engineering,
Purdue University,
West Lafayette, IN 47907
e-mail: shangw@purdue.edu

Yung C. Shin[1]
Fellow ASME
School of Mechanical Engineering,
Purdue University,
West Lafayette 47907
e-mail: shin@purdue.edu

Jun Chen
School of Mechanical Engineering,
Purdue University,
West Lafayette, IN 47907
e-mail: junchen@purdue.edu

Modeling Particle Spray and Capture Efficiency for Direct Laser Deposition Using a Four Nozzle Powder Injection System

Powder capture efficiency is indicative of the amount of material that is added to the substrate during laser additive manufacturing (AM) processes, and thus, being able to predict capture efficiency provides capability of predictive modeling during such processes. The focus of the work presented in this paper is to create a numerical model to understand particle trajectories and velocities, which in turn allows for the prediction of capture efficiency. To validate the numerical model, particle tracking velocimetry (PTV) experiments at two powder flow rates were conducted on free stream particle spray to track individual particles such that particle concentration and velocity fields could be obtained. Results from the free stream comparison showed good agreement to the trends observed in experimental data and were subsequently used in a direct laser deposition (DLD) simulation to assess capture efficiency and temperature profile at steady-state. The simulation was validated against a single track deposition experiment and showed proper correlation of the free surface geometry, molten pool boundary, heat affected zone boundary, and capture efficiency. [DOI: 10.1115/1.4038997]

Keywords: laser direct deposition, powder flow, capture efficiency, numerical modeling

Introduction

In recent years, additive manufacturing (AM) has gained a lot of interest as a technology for both component manufacturing and remanufacturing processes. One of the technologies in AM is direct laser deposition (DLD), which uses a mixture of powdered materials carried by a carrier gas to the molten pool on a substrate [1]. DLD processes, including laser engineered net shaping (LENS), allow complex components to be manufactured where typical manufacturing processes cannot provide [2]. Figure 1 provides a general diagram for the DLD process using a quadruple nozzle deposition head, as seen on the Optomec LENS 750 system, displaying only a cross section of the nozzle parallel to the direction of travel.

Efficiency of DLD processes is highly sensitive to the powder flow characteristics, since the amount of powder absorbed into the molten pool directly impacts track geometry and deposition quality. Typical control of powder flow is completed via changing powder mass feed rate, nozzle exit velocity, shielding gas velocity, and/or standoff distance [3]. For particles not absorbed into the molten pool, either directly or indirectly, a powder reclamation process must be performed to ensure particles being refed into the machine are of an appropriate size and composition. This process, unfortunately, may not allow all the recycled powder to be used or becomes particularly difficult in the case of different constituent powders being mixed together (i.e., when creating a functionally graded material or a composite material). Therefore, the most proactive approach to minimizing the time and cost of the laser additive process becomes maximizing the powder capture efficiency. Capture efficiency is a function of the mass concentration of the metal particles above the substrate surface, the particle velocity as they impact the molten pool, and the temperature and geometry of the molten pool [4]. Thus, if each of these quantities is known, the capture efficiency can be estimated using a physical model describing the deposition process once particle interactions at the surface can be quantified.

Several attempts at describing the powder flow distribution have been made on various nozzle geometries, including both coaxial nozzles and multinozzle configurations [5–13]. Although the physical phenomena of the problem at hand are similar in nature to such previously studied geometries, intricacies associated with particle interaction with the molten pool at the substrate surface, which play a critical role in assessing the capture efficiency, were not addressed in the previous studies. Moreover, the focus of most studies has been centered on a coaxial powder nozzle, which is a simpler configuration when compared to nozzle-based powder deposition. Unlike geometries, which may be reduced in dimensionality, nozzles such as the one at hand must be analyzed in three dimensions, with at most two symmetry planes to reduce the size of the domain.

Researchers have been developing models for specific nozzle arrangements and using such information for simulation of

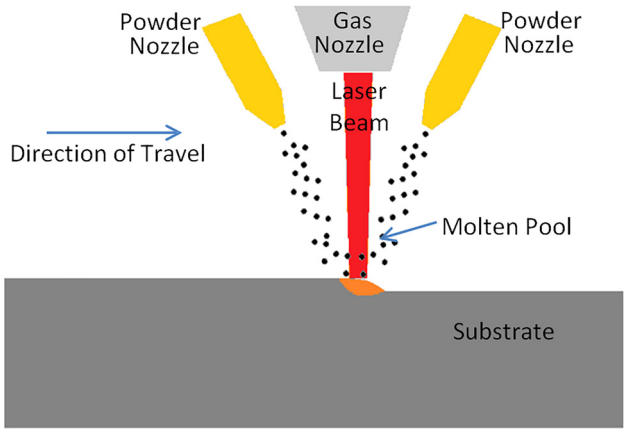

Fig. 1 Diagram of DLD process

[1]Corresponding author.

Manuscript received June 12, 2017; final manuscript received January 3, 2018; published online February 14, 2018. Assoc. Editor: Hongqiang Chen.

deposition processes. For example, Wen and Shin [12,14] created a powder flow distribution based on computational fluid dynamics (CFD) modeling, though only free stream interactions were modeled since particles were found to not be affected by the local gas flow field. Many researchers have indicated that bouncing particles play a significant role by providing mass addition into the molten pool without affecting the laser energy reaching the surface [7], though quantification of the amount of absorbed powder from reflection has yet to be established. Zekovic et al. [13] experimented on a four nozzle system similar in nature to the Optomec LENS 750 nozzle and utilized the collected information to produce a model to predict the powder concentration and gas velocity fields. Experimentation utilized a continuous wave laser to image the particles, allowing for the overall path traversed by the particles, without acquiring data from individual particles, which prevented the possibility of calculating localized powder velocity from experimental data. The assumptions made during the modeling effort were reasonable; however, the comparison between model prediction and experimental observation was limited to powder concentration, which is only one variable in obtaining insight into capture efficiency.

The prediction of capture efficiency ultimately enables a more representative model of the DLD process by only allowing particles, which would be trapped in the molten pool to be added to the simulated track. Ibarra-Medina et al. [7] have established a combined three-phase model to predict the powder flow of a coaxial nozzle onto a stainless steel substrate. In their study, capture efficiency was solved simultaneously with the molten pool dynamics, which were captured using full fluid dynamics equations coupled with volume of fluid for tracking the metal/gas interface. The concept of simulating the entire deposition domain was demonstrated successfully, though the demonstrated powder feed rate was at 0.168 g/min, which is a very low powder feed rate for DLD processes [15]. In a separate comparison, this time with experimental data and a higher powder feed rate, a single track simulation correlated well with experimentally acquired track height; however, the simulation yielded a semicircular cross section for the final track geometry, whereas it was observed to be trapezoidal in experimentation.

The focus of this investigation was to develop a computational fluid dynamics model to predict the particle spray pattern from a quadruple nozzle system and validate the prediction using pulsed laser particle tracking velocimetry (PTV). Using this model, particle interactions at the substrate surface were obtained such that a boundary condition for DLD simulation can be implemented to predict powder capture efficiency, which has been validated separately through DLD experimentation. Novelty in this work is demonstrated through the particle-based tracking method to create a powder concentration map, which is then used to determine capture efficiency via DLD model prediction. The results presented will be qualitatively correct for similar four nozzle systems, and since manufacturing differences in nozzles will exist, it becomes necessary to assess the impact of these differences on a case-by-case basis. The method presented in this paper could similarly be utilized for coaxial nozzles, though characterization of a more complex system (quad nozzles as compared to coaxial nozzles) demonstrates fullest capability of the method.

Experimental Setup

Particles of H13 powder were sieved to acquire a measurement on the size distribution such that a discrete phase model (DPM) could be implemented with minimal assumptions. A sample of 516.296 g of H13 powder from Carpenter Powder Products (Bridgeville, PA, Micro Melt H13 powder [–170 + 325 mesh]) was manually sieved through four mesh sizes (45 μm, 75 μm, 90 μm, and 150 μm) to acquire the mass within each size range. Table 1 provides the mass distribution of the tool steel particles from the sieve analysis. The mass fractions were fitted to a Rosin–Rammler distribution [16], as shown in Eq. (1):

Table 1 Mass distribution of H13 powder based on sieve analysis

Size (μm)	Mass collected (g)	% mass
x > 150	0.038	0.007%
90 < x < 150	140.766	27.323%
75 < x < 90	348.791	67.701%
45 < x < 75	20.012	3.884%
x < 45	5.586	1.084%
Total	**515.193**	

$$Y_d = e^{-(d/d_c)^n} \tag{1}$$

where d_c is the mean particle diameter (corresponding to Y_d=36.8%) and was found to be 88 μm, and n is the distribution spread factor which was calculated to be 10.75. Approximately 1.1 g (or 0.2%) of the powder mass is unaccounted for by the sieving; however, the amount of mass lost would minimally impact the mass distribution calculated by Eq. (1).

Figure 2 shows representative particles from each size range collected after sieving by viewing under an optical microscope (Nikon Eclipse LV150) at 5× magnification with identical magnification used for each image. For each size of particle collected, it can be seen that the approximate shape of each is similar, allowing for a constant shape factor, or the departure of the average particle shape from spherical, as a function of particle size.

The nozzle being studied in this analysis is the factory-installed quadruple nozzle of the Optomec LENS 750 machine. Figure 3 provides scaled pictures of the nozzle head containing four radially symmetric powder nozzles, and a center nozzle through which shielding gas is forced. Powder nozzles are each angled

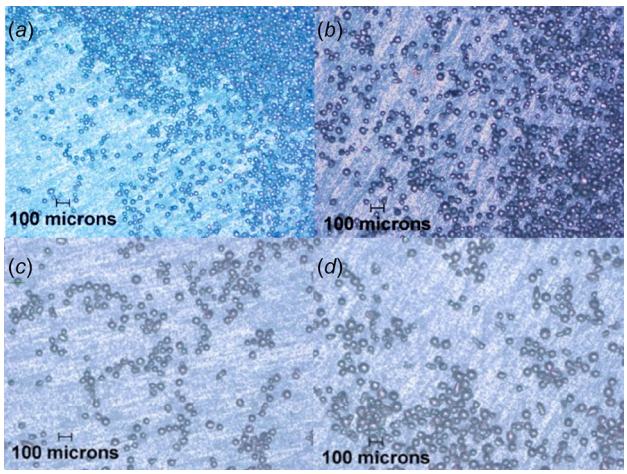

Fig. 2 H13 particle shapes at (*a*) <45 μm, (*b*) 45 μm < x < 75 μm, (*c*) 75 μm < x < 90 μm, and (*d*) 90 μm < x < 150 μm

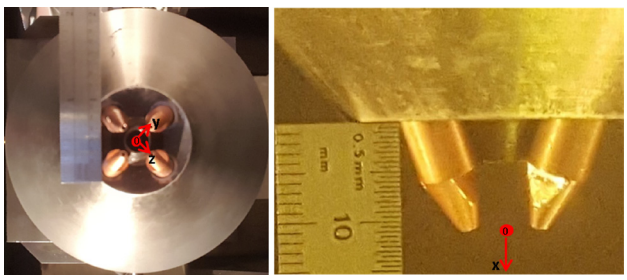

Fig. 3 Optomec LENS 750 nozzle geometry—bottom view (left) and side view (right)

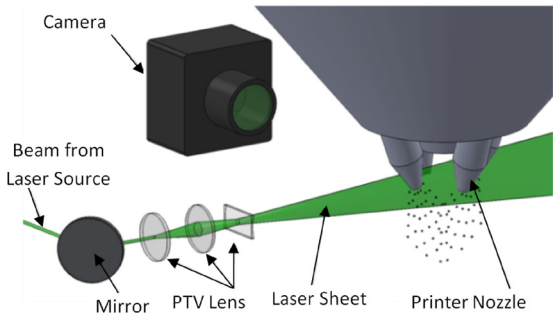

Fig. 4 Experimental setup of PTV equipment

approximately 23.2 deg from the laser beam axis. The flow path through the nozzles starts at 2.5 mm in diameter and tapers to an outlet diameter of 1.0 mm over a distance of 24.6 mm. The origin for the x-coordinate used in all figures is displayed in the side view and is zero at a plane corresponding to the four nozzle outlets.

A total of four experiments were performed to understand the impact of particle dynamics for two powder mass flow rates in both free stream and substrate impingement scenarios. Free stream particle trajectories are typically not used in standard manufacturing processes, since it denotes a lack of substrate being deposited on; however, results from such experimentation provide insight into the location of the first interaction of powder particles and the substrate. Impingement experimental data is representative of the deposition process since particles will reflect off of the substrate and can potentially land on the top of the molten pool.

During experimentation, the gas flow rate for both the shielding and assist gas was held constant at 13 standard liters per minute (SLPM), with 4.5 SLPM being diverted specifically for particle propulsion through the four powder feed nozzles. Although the typical carrier gas within the Optomec LENS 750 system is argon, PTV experimentation required the chamber to be exposed to atmospheric conditions, which requires adjustment when developing predictions of the powder distribution during deposition in an oxygen-depleted environment. A series of calibration experiments were performed to ensure the mass flow rate of particles from the nozzles could be quantified, and the two mass flow rates used were 9.84 ± 0.02 g/min and 6.55 ± 0.15 g/min, for hopper motor speeds of 7.5 rpm and 5.0 rpm, respectively.

A diagram for the setup of the PTV equipment is shown in Fig. 4. The laser sheet was generated using a Quantel USA pulse laser (532 nm) controlled by a Quantum Composers model 9518 pulse generator. An Imperx ICL-B4020M-KF000 digital camera with a Nikon AF Micro Nikkor 105 mm 1:2.8 D lens captured images based on a trigger from the pulse generator. The laser sheet illuminated the $z = 0$ plane, which crosses the centers of the two out-of-plane nozzles. A pulse spacing of 35 μs was utilized such that at least 10 pixels of particle travel could be observed in the region of interest between adjacent images. Calibration of the image window resolution was performed using a Newport Resolution RES-1 Target, providing a scaling factor of 46 pixels per millimeter. An in-house developed PTV software was used to analyze the velocity of each captured particle (v) by determining its travel distance, Δx, such that $v = \Delta x/\Delta t$, where Δt is the time between images (35 μs).

Upon capturing 880 images at each experimental condition, the particle velocity field was acquired by assigning a velocity at each particle location. Figure 5 shows the obtained particle velocity field in a free stream particle flow scenario at a powder mass flow rate of 9.84 g/min by agglomerating all 880 images to increase particle density for better visualization. In free stream flow, particles travel in the downward direction regardless of the originating nozzle, and thus, they can be identified via directionality of the trajectory and are ignored in the event that the velocity vector points toward the nozzles. To more clearly observe the origin of each particle, the velocity vectors have been color coordinated based on the nozzle from which the particle was ejected, with the center set of vectors denoting particles from the combination of both out-of-plane nozzles. Additionally, a contour plot of the average velocity magnitude over 16×16 pixel areas was created and shows the highest velocity magnitude to be associated with particles along the nozzle axis.

In the impingement case, however, once a particle has impacted the substrate, it will deflect based on the interaction between the particle and the substrate, whether it is full or partial reflection from the surface. In the region adjacent to the substrate, PTV was unable to capture a reasonable trend due to the particle scatter at the impingement point, though, based on observation during experiments, powder reflection prevented accumulation adjacent to the molten pool, indicating that only powder particles which have trajectories directly from the nozzles to the molten pool need to be considered. For particle and gas properties similar to those used in this experimentation, Wen et al. [14] showed that particles

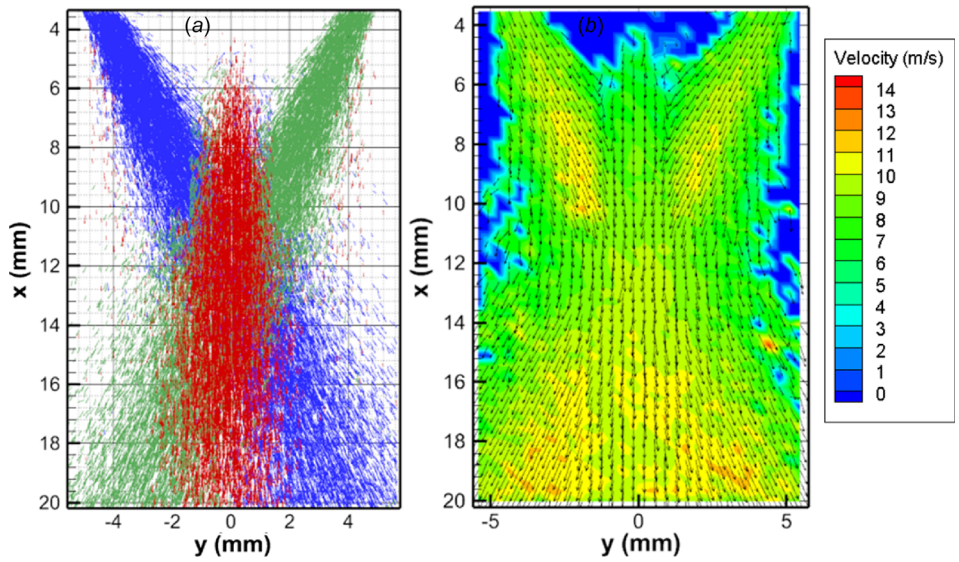

Fig. 5 Particle velocity field for free stream experimentation at 7.5 rpm hopper speed: (*a*) individual particles colored by originating nozzle and (*b*) average overall particle velocity field

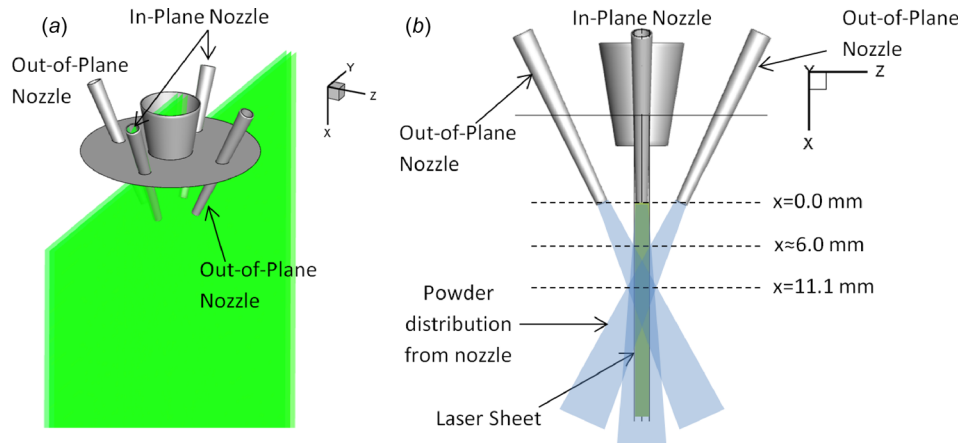

Fig. 6 Detail of particle interaction with laser sheet (*a*) isometric view and (*b*) side view

are not influenced by the gas velocity field, indicating that trajectories can be obtained from free stream simulation data at the corresponding stand-off distance.

Figure 6 depicts a diagram of the interaction of the particles emerging from the out-of-plane nozzles with the laser sheet. The laser sheet resides within the x-y plane; hence, PTV provides a cross-sectional view of the in-plane powder nozzles, while only providing a limited view of the particles emerging from the two out-of-plane nozzles. Only select particles from the four nozzles will interact with the laser sheet, and thus, a slice of the particle cloud with finite thickness is collected from the experimental data. The thickness of the slice can be determined by the extent in which out-of-plane nozzle particles can be observed in the PTV imagery. For example, in Fig. 5, few particles above $x = 6.0$ mm were observed in experimentation. Since the laser sheet thickness is less than that of the entire nozzle, only particles below a certain x-coordinate will interact with the laser sheet, as indicated in Fig. 6. By modeling the spread of particles which emerged from the two in-plane nozzles (since out-of-plane nozzles do not interact with the nozzle sprays from the two in-plane nozzles), and using the same parameters for both of the out-of-plane nozzles, slices of the particle concentration may be obtained at various planes parallel to the laser sheet. Correlation of the laser sheet thickness to the experimental data is performed by assessing the concentration of particles which were detected by the laser sheet and comparing against the modeled version of the same system.

Particle concentration can be obtained from the experimental results by counting the average number of particles within an 8×8 pixel window over the 880 images and calculating a weighted density based on a linear ratio between the volume of free air contained within the laser sheet and the volume of spherical particles with the density of tool steel. Diameters of the individual particles were determined using the number of pixels illuminated for a given particle, and calculating the diameter (in pixels) assuming an equivalent circular cross-sectional shape using the scaling factor. Figure 7 depicts the particle concentrations calculated from the experimental data of the free stream scenario at a 9.84 g/min powder feed rate.

Experimentation of the deposition process was performed using an H13 tool steel substrate with Micro Melt H13 powder. Operating parameters of the Optomec LENS 750 included a laser power of 350W with laser waist diameter of 0.66 mm, scanning speed of 14.82 mm/s, and a powder feed rate of 8.5 g/min. A series of 51 mm single tracks were deposited onto the substrate and cut perpendicular to the laser scanning direction to gain access to the cross section of the sample. Then the sample was cured within Bakelite thermosetting resin, polished down to 6 μm diamond, and etched with a 5% Nital solution to expose the microstructure of the heat affected zone. Figure 8 shows a representative track cross section with the track geometry, and molten pool

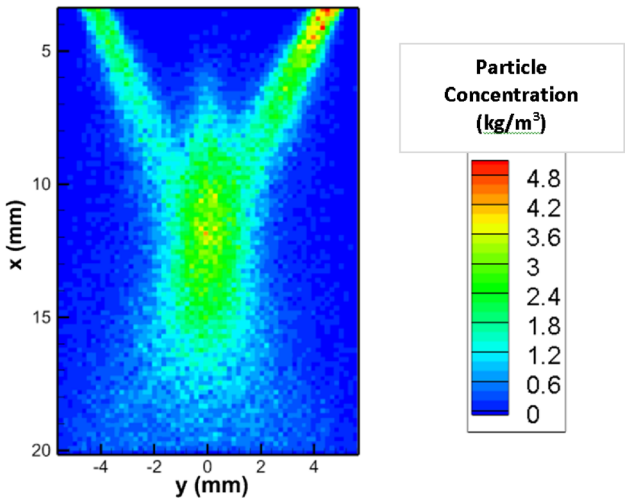

Fig. 7 Particle concentration for free stream at 9.84 g/min

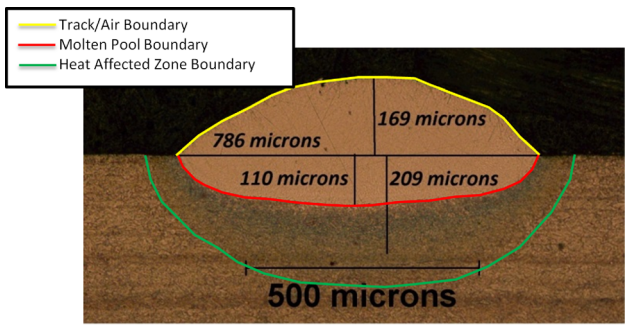

Fig. 8 Cross section view of single track H13 deposition

($T_{solidus}$=1588 K) and heat affected zone ($T_{austenite}$=1023 K) boundaries accentuated.

Analysis

Powder Flow Modeling: Equations. The governing equations describing the bulk fluid flow within the domain are given by continuity, momentum, and turbulence. In addition, a discrete phase model is used to account for the effect of local velocity on the metal particles. Because this physical system is turbulent in nature and turbulence is a three-dimensional phenomenon, all governing

equations presented require a solution in a three-dimensional domain, which are solved by using FLUENT.

Governing equations for continuity and momentum are shown in Eqs. (2) and (3) [12], respectively,

$$\frac{\partial \rho}{\partial t} + \nabla \cdot (\rho \boldsymbol{V}) = 0 \tag{2}$$

$$\frac{\partial (\rho \boldsymbol{V})}{\partial t} + \nabla \cdot (\rho \boldsymbol{V}\boldsymbol{V}) = -\nabla P + \nabla \cdot (\bar{\bar{\tau}}) + \boldsymbol{S}_{\text{dpm}} \tag{3}$$

where $\bar{\bar{\tau}}$ is the stress tensor as shown in Eq. (4), P represents the pressure, and $\boldsymbol{S}_{\text{dpm}}$ is the force coupling from the discrete phase model. It is assumed that due to the low concentration of particles with respect to the gas, one-way coupling is valid, and thus the gas affects the discrete phase, not vice versa (i.e., $\boldsymbol{S}_{\text{dpm}} = 0$)

$$\bar{\bar{\tau}} = \mu \left[(\nabla \boldsymbol{V} + \nabla \boldsymbol{V}^{\boldsymbol{T}}) - \frac{2}{3} \nabla \cdot \boldsymbol{V} \boldsymbol{I} \right] \tag{4}$$

In Eq. (4), μ is the viscosity and $\boldsymbol{I}$ is the identity matrix.

A standard k-ε turbulence model is utilized to capture time-average flow fields, as was developed by Launder and Spalding [17], and is provided in Eqs. (5) and (6)

$$\frac{\partial (\rho k)}{\partial t} + \frac{\partial (\rho k \mathbf{V}_i)}{\partial \mathbf{x}_i} = \frac{\partial}{\partial \mathbf{x}_j} \left[\left(\mu + \frac{\mu_t}{\sigma_k} \right) \frac{\partial k}{\partial \mathbf{x}_j} \right] + G_k + G_b - \rho \varepsilon - Y_M + S_k \tag{5}$$

$$\frac{\partial (\rho \varepsilon)}{\partial t} + \frac{\partial (\rho \varepsilon \mathbf{V}_i)}{\partial \mathbf{x}_i} = \frac{\partial}{\partial \mathbf{x}_j} \left[\left(\mu + \frac{\mu_t}{\sigma_\varepsilon} \right) \frac{\partial \varepsilon}{\partial \mathbf{x}_j} \right] + C_{1\varepsilon} \frac{\varepsilon}{k} (G_k + C_{3\varepsilon} G_b) - C_{2\varepsilon} \rho \varepsilon \frac{\varepsilon}{k} + S_\varepsilon \tag{6}$$

where coefficients $C_{1\varepsilon}$=1.44, $C_{2\varepsilon}$=1.92, $C_{3\varepsilon}$=0.0, C_μ=0.09, σ_k=1.0, and σ_ε=1.3, based on default values in FLUENT since these parameters provide reasonable estimation of turbulence for jet flows [16], G_b is the generation of turbulent kinetic energy from buoyancy, G_k is the generation of turbulent kinetic energy from average velocity gradients, S_ε and S_k are user-defined (both set to zero) and μ_t is the turbulent viscosity. Calculations of remaining source terms within the turbulence equations are documented in the FLUENT theory guide [16]. Near-wall treatment is handled using enhanced wall treatment, which separates wall interactions into two layers based on a nondimensional wall distance and using a blending function [18] to smoothly link the laminar and turbulent regimes together.

The discrete phase model is governed by trajectory motion of point masses via a force balance as shown by Eq. (7) [16]

$$\frac{\partial \mathbf{u}_p}{\partial t} = F_D (\boldsymbol{V} - \mathbf{u}_p) - \frac{\mathbf{g}_x (\rho - \rho_p)}{\rho_p} + \mathbf{F}_x \tag{7}$$

where F_D is a velocity damping term including effects for aerodynamic drag of a given particle and $\mathbf{F}_x$ includes additional particle body forces, which are zero for this study. The drag coefficient is a function of the particle size, shape, density, and the viscosity of the working fluid, as shown in Eq. (8). Velocity values used to calculate Reynolds number are based on the magnitude of the relative velocity between a given particle and the gas phase velocity

$$F_D = \frac{18 \mu_g}{\rho_p d_p^2} \frac{C_d \text{Re}}{24} \tag{8}$$

Nonspherical particles were discovered upon inspection of the sieve analysis, and hence it is necessary to model the departure of simulated particle shapes from spheres. A shape factor is used to describe such nonideality, as shown in Eq. (9):

$$\phi = \frac{A_{\text{sph}}}{A_p} \tag{9}$$

where A_p is the surface area of the actual particles and A_{sph} is the surface area of a sphere with the same volume as the particle. Based on visual comparison as in the previous work [14] in addition to estimation of particle surface area and volume, a shape factor of 0.8 reasonably describes the H13 particles. The coefficient of drag must include the effect of nonspherical particles, and is shown in Eq. (10) [19].

$$C_d = \frac{24}{\text{Re}} (1 + a_1 \text{Re}^{a_2}) + \frac{a_3 \text{Re}}{a_4 + \text{Re}} \tag{10}$$

where

$$a_1 = \exp(2.33 - 6.46\phi + 2.45\phi^2) \tag{11}$$

$$a_2 = 0.096 + 0.56\phi \tag{12}$$

$$a_3 = \exp(4.91 - 13.89\phi + 18.42\phi^2 - 10.26\phi^3) \tag{13}$$

$$a_4 = \exp(1.47 + 12.26\phi - 20.73\phi^2 + 15.89\phi^3) \tag{14}$$

The Stokes number was calculated to understand the effect of gas velocity on H13 particles for the two size extremes, 45 μm and 150 μm, and was calculated based on Eq. (15)

$$St = \frac{u_o}{l_o} \frac{\rho_d d_d^2}{18 \mu_g} \tag{15}$$

where d_d is the particle diameter, ρ_d is the particle density, μ_g is the dynamic viscosity of the carrier gas, u_o is the local gas velocity, and l_o is the characteristic length of an obstacle. For the smallest particle diameter (45 μm) of H13 with a density of 7835 kg/m^3, carried by air with a viscosity of 1.849×10^{-5} kg/m s and velocity of 10 m/s by a nozzle with radius of 0.5 mm, the Stokes number is calculated to be 1.6×10^4, indicating the inertial effects are too large for the flow field to impact the particles.

Since the laser was deactivated during experimentation, the effect of the energy equation was assumed to be negligible for this system. Furthermore, due to the relatively low velocities of the shielding and assisting gas observed within the system, pressure effects on gas enthalpy due to stagnation can be neglected.

The equations described in this section are solved numerically using ANSYS FLUENT [16], a commercially available software package. Several assumptions have been made to both reduce computation time and minimize model tuning parameters: (1) Particles are assumed to be dilute with respect to the gas phase, allowing the interaction of particles with each other to be neglected. Furthermore, the particles are assumed to have a Rosin–Rammler distribution [16], as discussed earlier. (2) Energy due to laser irradiation is not included since the laser was deactivated during experimentation. (3) Although the flow is turbulent in nature, the flow field is solved as steady-state turbulent flow, thus providing an average glimpse into the flow field. (4) Since pressure drop within the flow is relatively low and the velocity is significantly below the Mach number for air at room temperature, the gas phase is assumed to be incompressible.

Direct Laser Deposition: Equations. Governing principles of the DLD process are conservation of mass, momentum, energy, and levelset, as shown in Eqs. (16) through (19) [12], respectively,

$$\frac{\partial \rho}{\partial t} + \nabla \cdot (\rho \boldsymbol{V}) = S_{\text{mass}} \tag{16}$$

$$\frac{\partial(\rho \boldsymbol{V})}{\partial t} + \nabla \cdot (\rho \boldsymbol{V}\boldsymbol{V}) = -\nabla P + \nabla \cdot (\bar{\bar{\tau}}) + \mathbf{S}_{\text{mom}} \tag{17}$$

$$\frac{\partial(\rho h)}{\partial t} + \nabla \cdot (\rho \boldsymbol{V} h) = \nabla \cdot (k \nabla T) + S_{\text{energy}} \tag{18}$$

$$\frac{\partial(\rho \varphi)}{\partial t} + \nabla \cdot (\rho \boldsymbol{V} \varphi) = S_{\text{levelset}} \tag{19}$$

As opposed to the powder flow modeling, when simulating the deposition process, laser irradiation to the substrate as well as scatter and attenuation of the laser beam due to particle energy absorption should not be neglected, and is thus included in the energy equation as a source term. The free surface of the substrate and deposited material is tracked using a levelset balance such that the free surface coincides with a levelset isocontour with a value of zero. Source terms in Eqs. (16) through (19), (S_{mass},S_{mom}, S_{energy}, and S_{levelset}), are sources due to the addition of powder to the free surface of the substrate, and will change throughout simulation. As the solution progresses, the location of the free surface can be monitored to properly distribute mass only at free surface locations. Wen and Shin have recast each source term such that all are functions of the levelset field. Further details of the laser deposition model can be found in Wen and Shin [12].

To handle capture efficiency of powder, a heuristic was implemented on the source terms to only allow addition of incoming powder when the combination of the molten pool and the impinging powder mass have sufficient thermal energy to maintain a temperature above the liquidus temperature of the material. If this condition is not met, the powder is reflected. This is a reasonable assumption since nonmelted powder will not be in the deposited tracks. Since the only material that could be added is above the surface of the substrate, the mass added to the system can be calculated using Eq. (20)

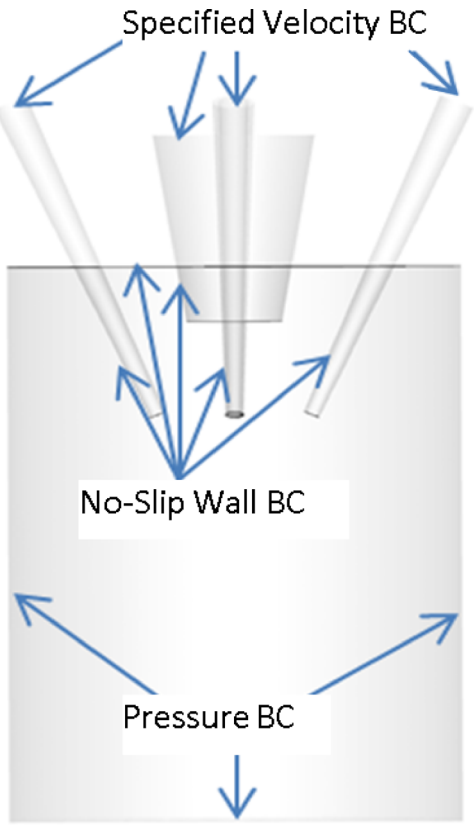

Fig. 9 Boundary conditions for free stream domain

Table 2 Thermal and physical properties of H13 tool steel

Property	Units	Solid phase	Liquid phase
Density	kg/m^3	7835 [20]	7835 [20]
Specific heat	J/kg K	658 [21]	804 [21]
Thermal conductivity	W/m K	28.6 [21]	28.6 [20]
Liquid viscosity	kg/m s	—	0.005 [21]
Thermal expansion coefficient	1/K	1.45×10^{-5} [21]	
Absorptivity	—	0.30 [22]	
Emissivity	—	0.70 [23]	
Latent heat	J/kg	2.72×10^5 [21]	
Solidus temperature	K	1588 [20]	
Liquidus temperature	K	1727 [20]	
Surface tension coefficient	N/m K	-4.3×10^{-4} [24]	

$$\dot{m}_{\text{capture}} = \rho v_{\perp} \int (H(x) - H_o) dx \tag{20}$$

where $v_{\perp}$ is the feed rate velocity, $\dot{m}$ is the calculated mass captured, ρ is the density of the feed powder, and $(H(x) - H_o)$ denotes the height of the track at a given location along the cross section. Once the captured mass is calculated, the capture efficiency can be determined via Eq. (21), by dividing the mass flow

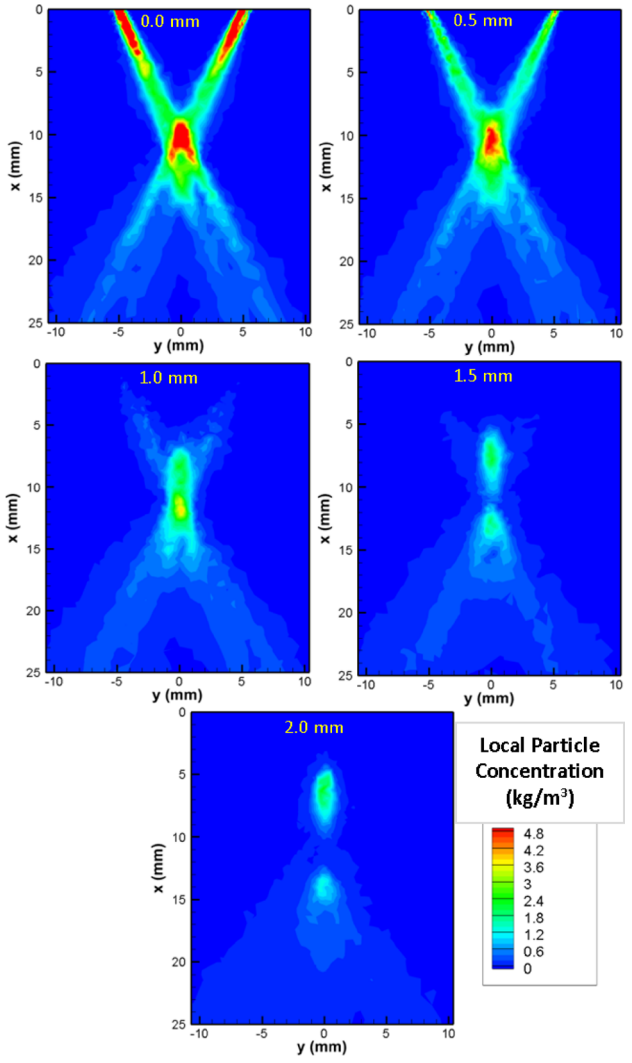

Fig. 10 DPM concentration at nozzle head off-axis slices from 0.0 mm to 2.0 mm at 9.84 g/min powder feed rate

rate of captured powder ($\dot{m}_{\text{capture}}$) by the mass flow rate of feed powder ($\dot{m}_{\text{feed}}$)

$$\eta_{\text{cap}} = \frac{\dot{m}_{\text{capture}}}{\dot{m}_{\text{feed}}} \tag{21}$$

Powder Flow Modeling: Method. The computational domain used in this study corresponds to the free stream case, and is composed of the four powder-carrying nozzles and the shielding gas nozzle with an attached gaseous region to allow for gas expansion upon exiting each of the nozzles. To minimize the computational domain, the gaseous region was truncated beyond 29.0 mm, or 2.6 powder nozzle focal distances based on the nozzle head geometry. This is reasonable since particles in the free stream case cannot reflect back into the domain and do not interact with each other. Boundary conditions for the computational domain are shown in Fig. 9. Wall boundaries within the nozzles are all assumed to be nonslip stationary walls, which reflect metal particles without momentum loss. At the powder nozzle inlets, a velocity normal to each face has an imposed gas velocity magnitude of 5.04 m/s and a particle velocity of 10.5 m/s with an additional 0.3 m/s tangential velocity to allow dispersal of the powder stream upon exit. Particle velocities were determined based on imaging studies of particles leaving the nozzles. The shielding gas nozzle has a uniform inlet velocity of 2.08 m/s. Pressure boundary conditions are all imposed at 0 Pa gauge pressure. The domain was composed of 2.159×10^6 computational cells, with the majority being tetrahedral control volumes.

The smallest computational volume (located near the focal point of the nozzles) had a side length of 65 μm, while the largest had a side length of 0.43 mm and was located near the circumference of the domain. A grid independence study was performed by increasing the number of control volumes to 3.315×10^6 and showed less than 2% variation on the maximum gas velocity with a refined mesh.

The domain was initialized with a static velocity field ($\boldsymbol{V}$=0), after which simulations continued until residuals stabilized below 1×10^{-4} for continuity, 1×10^{-6} for momentum, turbulent kinetic energy and turbulent dissipation, or until maximum velocity and average velocity near the focal point changed less than 0.025%, whichever occurred last. Prior to reviewing results, a final discrete phase model update was performed to acquire the latest information regarding the powder concentration and velocity.

Direct Laser Deposition: Method. Simulation of the DLD process was performed using a rectangular domain composed of a 12 mm × 5 mm × 12 mm gaseous domain above a 12 mm × 5 mm × 12 mm substrate discretized into 343,728 total control volumes. The mesh was arranged in a structured manner but with nonuniform grid spacing to acquire higher control volume count near the laser deposition location. Minimum control volume lengths are 33 μm in the depth direction of the substrate and 50 μm along the surface of the substrate. Thermal and physical properties of the H13 tool steel were selected based on values available in literature, and are shown in Table 2.

Initially, the substrate temperature was set to 300 K, and convective boundary conditions with a constant convection coefficient of 10 W/m K at 300 K ambient temperature were used for all faces of the substrate. A second-order implicit time advancement scheme was used to solve the governing equations for the deposition model, first by using a time-step of 5.0×10^{-6} s for

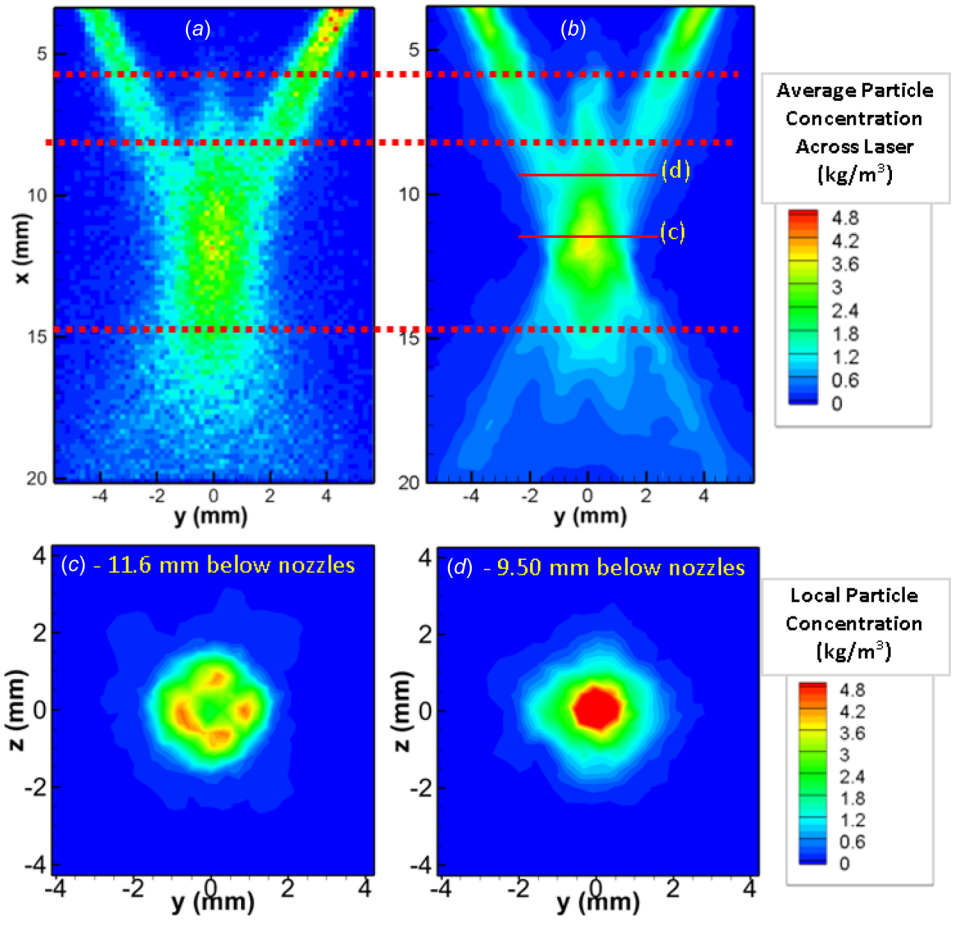

Fig. 11 Comparison of (*a*) experimental particle concentration and (*b*) modeled concentration with extracted concentration contours at two locations (9.84 g/min)

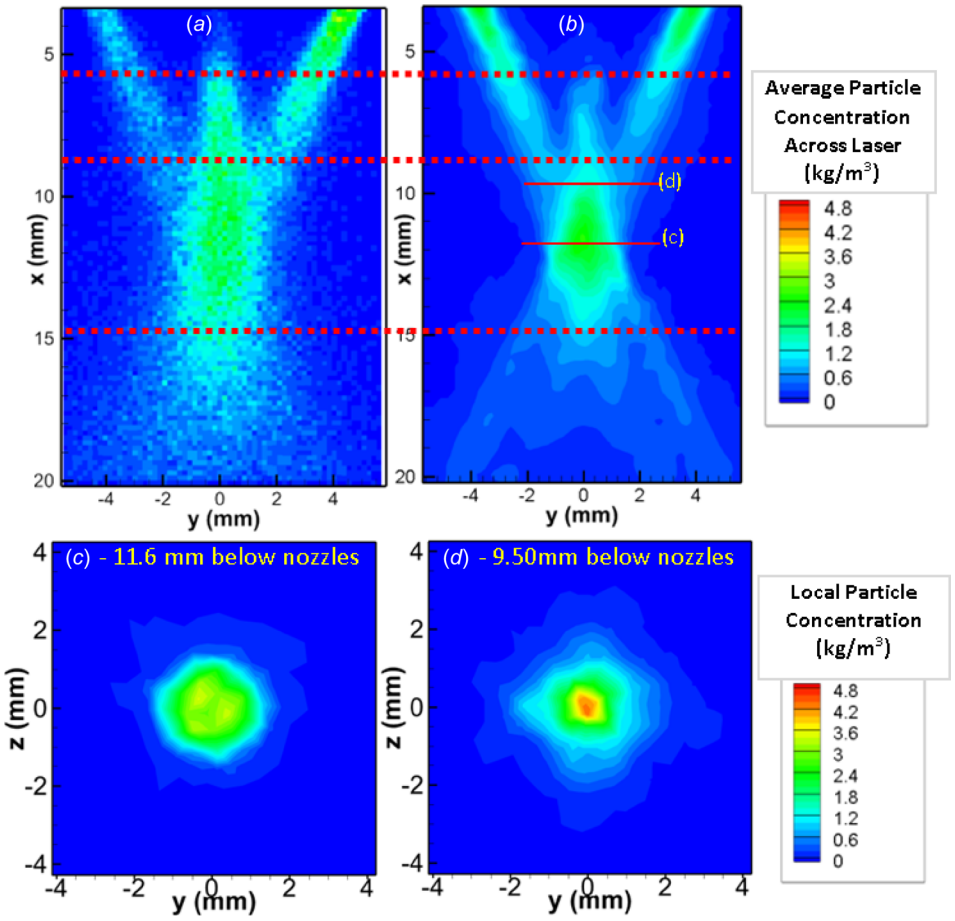

Fig. 12 Comparison of (*a*) experimental particle concentration and (*b*) modeled concentration with extracted concentration contours at two locations (6.55 g/min)

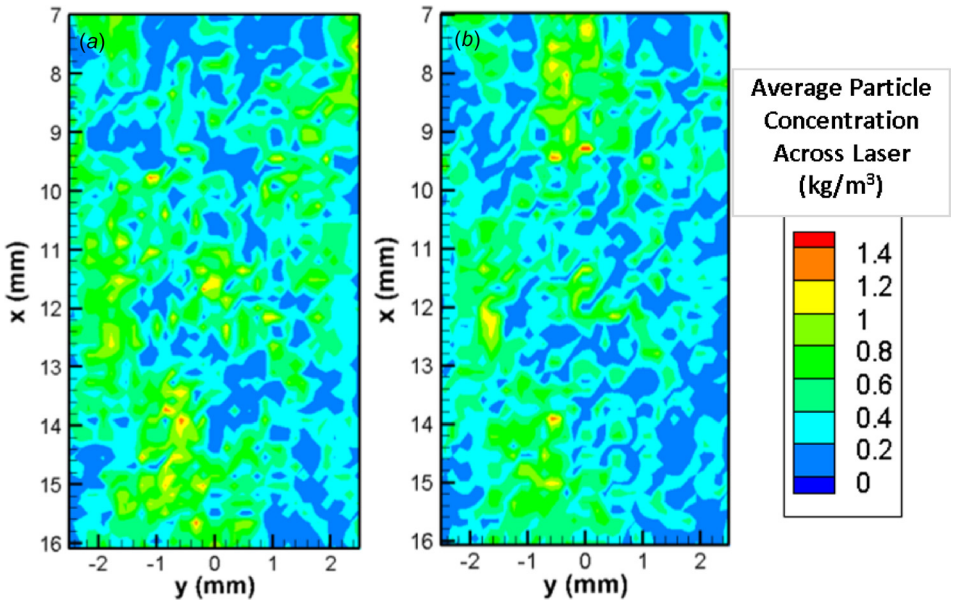

Fig. 13 Error quantification of free stream cases—powder feed of 9.84 g/min (*a*) and 6.55 g/min (*b*)

16,900 time steps (10 pseudo steps per time-step) to allow the solution to stabilize, then using a time-step of 2.0×10^{-5} s for 2440 time steps (10 pseudo steps per time-step). The simulation was stopped once the laser had traversed a distance of 1.98 mm.

Results and Discussion

Powder Flow Modeling. When observing the results obtained from PTV, particles from the two center nozzles can be seen

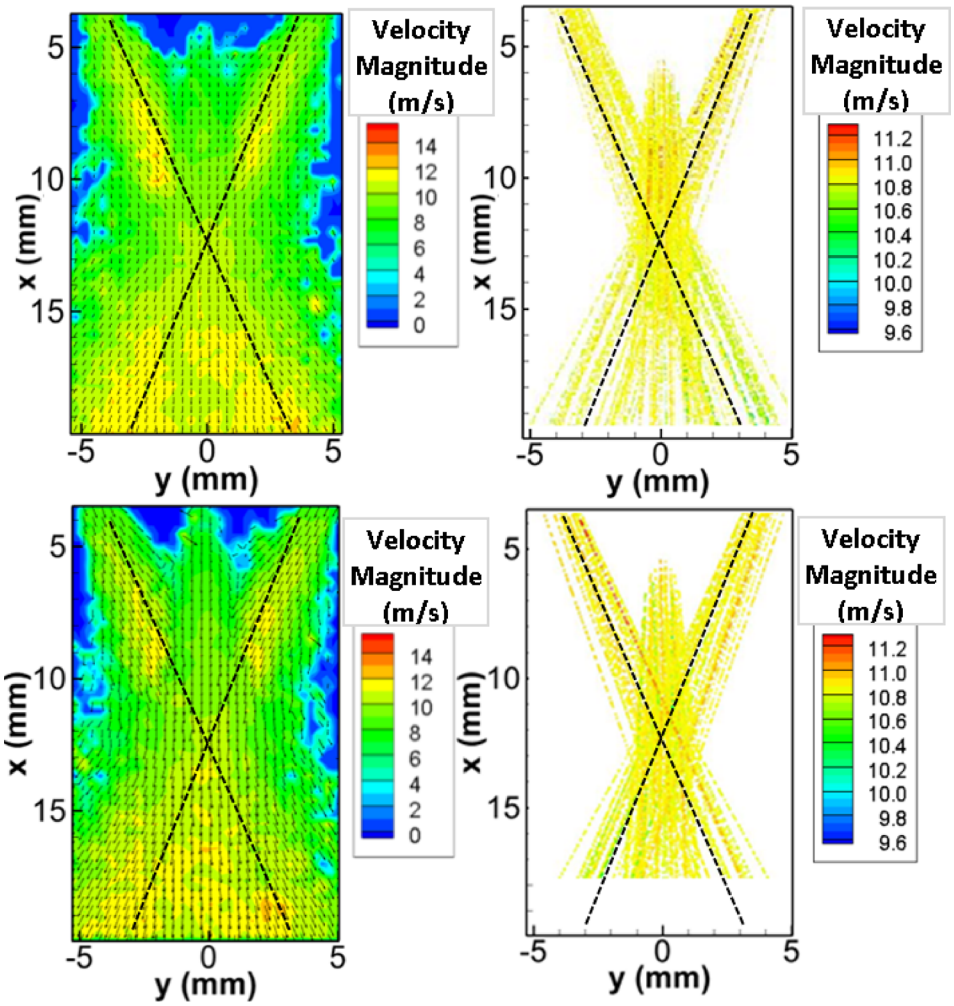

Fig. 14 Particle velocity fields for free stream scenario at 9.84 g/min (top) and 6.55 g/min (bottom) powder feed rates

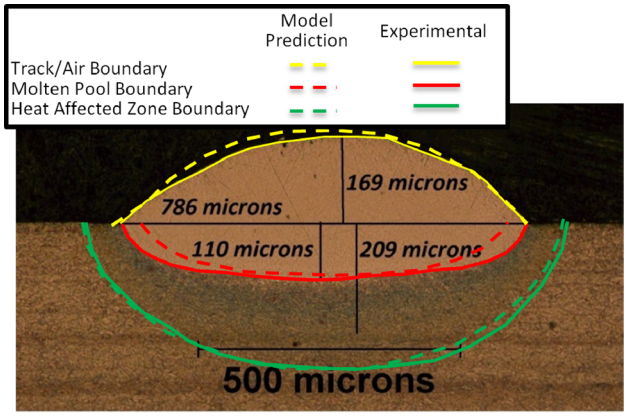

Fig. 15 Comparison of H13 tool steel DLD simulation results to experimental measurements

entering the domain above the nozzle focal point, as was seen in Fig. 5(*a*). It is believed the particles used in this experiment were reflective enough to scatter the illumination source within 2 mm of each direction the vertical center plane (equivalent laser sheet thickness of 4 mm). Consequently, comparison of simulation to experimental results requires an average particle concentration over the 4 mm effective laser sheet thickness.

To demonstrate the effect of effective laser sheet thickness, differences in the powder concentration profile can be seen by extracting slices from the simulation domain using parallel planes in 0.5 mm increments from the laser sheet center plane, as shown in Fig. 10. Starting at approximately 1.0 mm from the laser sheet center plane, the influence from the out-of-plane nozzles can initially be observed, while slices farther from the laser sheet center plane are predominantly governed by powder flow from the out-of-plane nozzles.

Two methods of comparison with regard to the powder flow field can be utilized to assess the accuracy of the numerical model: particle velocity and particle concentration. Figure 11 provides a comparison of the experimentally acquired particle concentration and the modeled results averaged over the effective laser sheet thickness for the higher powder flow rate case of 9.8 g/min in free stream flow. The general trend of the powder concentration predicted by the model matches that observed in experimentation. At each nozzle, the powder concentration diminishes due to conical expansion of the powder jet, until convergence of the four nozzles begins to occur (at approximately $x = 10$ mm), at which point the powder concentration reaches a localized maximum near the powder focal point and finally continues to diminish. Two cross-sectional planes of the powder concentration profile have been extracted and are shown as subfigures (*c*) and (*d*). The powder concentration contour shown at 11.6 mm corresponds to the location of the averaged powder concentration focal point while the contour plot at 9.5 mm corresponds to the plane of a typical stand-off used for this nozzle head during operation. Previous

experimentation has shown that more stable and consistent depositions are observed at standoff distances less than the averaged powder focal point [25], which is further validated with the local powder concentration being a maximum approximately 2.1 mm from above the averaged powder focal point.

Figure 12 depicts the experimental results and model prediction for powder flow in free stream with a powder flow rate of 6.55 g/min. As seen in the higher powder flow rate, the powder concentration decreases upon ejection from the nozzles, and as the powder streams converge, the particle concentration rises. The maximum particle concentration predicted in the 9.84 g/min and 6.55 g/min powder flow models are 8.89 kg/m^3 and 5.96 kg/m^3 at locations 2.1 mm above the averaged focal point, respectively. The ratio of the maximum particle concentration and powder feed rate between the two cases is similar, indicating linearity of the particle concentration and the powder flow rate.

A contour of the absolute difference of the powder concentration between experimentation and simulation was created in the powder focal region and plotted in Fig. 13. From the error plots, the discrepancy is mostly scattered and random, with a maximum of 1.46 kg/m^3 for the higher feed rate (average error is 0.394 kg/m^3) and 1.47 kg/m^3 for the lower feed rate (average error is 0.338 kg/m^3). The checkerboarding pattern observed in the error plots is due to the pixelation of the experimental data.

To complete the information necessary for modeling of the deposition process, the particle velocity is compared against experimental results to assess general trends in the particle velocity field. Using a discrete phase model within FLUENT, path traces were investigated. Figure 14 shows the particle velocity field calculated from experimentation along with particle tracks colored by velocity. Although the velocity magnitude is of the same order of magnitude (approximately 10.8 m/s uniform velocity profile), trends at the focal point of the powder cannot easily be discerned. Since experimental results provided an averaged observed set of particles, whereas FLUENT provides a single average snapshot of the particles within the domain, comparison of the velocity fields remains qualitative.

Direct Laser Deposition. Using the powder concentration and velocity, a source term for the levelset function was identified. Figure 15 shows the steady-state results for the track profile, heat affected zone, and molten pool with a comparison to the extracted boundaries previously shown in Fig. 8. The track width and height were extracted from the cooled region in the model and were found to be 802 μm and 174 μm, respectively, compared to 786 μm and 169 μm from the experimental track, resulting in an error of 2% and 3% for the track width and height, respectively. Calculating the capture efficiency using Eqs. (20) and (21) resulted in a 7.5% capture rate in experimentation compared to 7.7% from simulation, or a 2.6% difference.

The heat-affected zone, corresponding to the austenitic transformation temperature of H13 (T = 1023 K), was compared against a curve created from observation of the microstructure via optical microscopy, and was found to match both with respect to size and shape. Finally, for the molten pool region (T = 1588 K), the shape was found to be sufficiently close, though the width of the molten pool was found to be 40 μm less than the molten pool observed experimentally, or a 5% deviation. A laser beam diameter of 0.66 mm was modeled, but uncertainty exists depending on actual lens distance from the substrate. Nonetheless, modeling results show good correlation to all three validation points from the experimental data.

Conclusions

A computational fluid dynamics model to describe the particle concentration was developed for the four nozzle system found in an Optomec LENS 750 machine and has been shown to provide predictive capability of the particle concentration and velocity. Error between the developed model and experimental data was quantified for two powder flows and showed a deviation of approximately 15% in particle concentration. Using the results from the CFD model, the powder concentration and velocities were used as boundary conditions in a direct laser deposition model to assess capture efficiency, which predicted the track height and width within 3% of experimentally observed values and predicted shape and size of the molten pool within 5% of experimental results. Both shape and size of the heat affected zone matched observations, although there is some degree of uncertainty in clearly identifying the boundary. From the track geometry prediction, capture efficiency was calculated and found to deviate 2.6% from experimental capture efficiency.

Funding Data

- National Science Foundation (Grant No. CMMI-1233783).

References

[1] Irving, R., 1999, "Taking a Powder," Mech. Eng., **121**(9), p. 55.
[2] Keicher, D. M., and Miller, W. D., 1998, "LENS^{TM} Moves Beyond Rp to Direct Fabrication," Met. Powder Rep., **12**(53), pp. 26–28.
[3] Mazumder, J., 1996, "Laser Assisted Surface Coatings," *Metallurgical and Ceramic Protective Coatings*, Chapman and Hall, London, pp. 74–111.
[4] Partes, K., 2009, "Analytical Model of the Catchment Efficiency in High Speed Laser Cladding," Surf. Coat. Technol., **204**(3), pp. 366–371.
[5] Pinkerton, A. J., and Li, L., 2004, "Modelling Powder Concentration Distribution From a Coaxial Deposition Nozzle for Laser-Based Rapid Tooling," ASME J. Manuf. Sci. Eng., **126**(1), pp. 33–41.
[6] Lin, J., 2000, "Numerical Simulation of the Focused Powder Streams in Coaxial Laser Cladding," J. Mater. Process. Technol., **105**(1), pp. 17–23.
[7] Ibarra-Medina, J., Vogel, M., and Pinkerton, A. J., 2011, "A CFD Model of Laser Cladding: From Deposition Head to Melt Pool Dynamics," 30th International Congress on Applications of Lasers and Electro-Optics (ICALEO), Orlando, FL, Oct. 23–27, pp. 23–27.
[8] Yang, N., 2009, "Concentration Model Based on Movement Model of Powder Flow in Coaxial Laser Cladding," Opt. Laser Technol., **41**(1), pp. 94–98.
[9] Lin, J., and Steen, W. M., 1997, "Powder Flow and Catchment During Coaxial Laser Cladding," Proc. SPIE, **3097**, pp. 517–528.
[10] Thakar, Y. D., Pan, H., and Liou, F., 2004, "Numerical and Experimental Analysis of the Powder Flow Streams in the Laser Aided Material Deposition Process," 15th Conference on Solid Freeform Fabrication (SFF), Austin, TX, Aug. 2–4, pp. 512–522.
[11] Yang, S., and Evans, J., 2007, "Metering and Dispensing of Powder; the Quest for New Solid Freeforming Techniques," Powder Technol., **178**(1), pp. 56–72.
[12] Wen, S., and Shin, Y. C., 2010, "Modeling of Transport Phenomena During the Coaxial Laser Direct Deposition Process," J. Appl. Phys., **108**(4), p. 044908.
[13] Zekovic, S., Dwivedi, R., and Kovacevic, R., 2007, "Numerical Simulation and Experimental Investigation of Gas–Powder Flow From Radially Symmetrical Nozzles in Laser-Based Direct Metal Deposition," Int. J. Mach. Tools Manuf., **47**(1), pp. 112–123.
[14] Wen, S., Shin, Y., Murthy, J., and Sojka, P., 2009, "Modeling of Coaxial Powder Flow for the Laser Direct Deposition Process," Int. J. Heat Mass Transfer, **52**(25), pp. 5867–5877.
[15] Thompson, S. M., Bian, L., Shamsaei, N., and Yadollahi, A., 2015, "An Overview of Direct Laser Deposition for Additive Manufacturing; Part I: Transport Phenomena, Modeling and Diagnostics," Addit. Manuf., **8**, pp. 36–62.
[16] ANSYS, 2009, "Fluent 12.0 Theory Guide," Ansys Inc., Canonsburg, PA.
[17] Launder, B. E., and Spalding, D., 1974, "The Numerical Computation of Turbulent Flows," Comput. Methods Appl. Mech. Eng., **3**(2), pp. 269–289.
[18] Kader, B., 1981, "Temperature and Concentration Profiles in Fully Turbulent Boundary Layers," Int. J. Heat Mass Transfer, **24**(9), pp. 1541–1544.
[19] Haider, A., and Levenspiel, O., 1989, "Drag Coefficient and Terminal Velocity of Spherical and Nonspherical Particles," Powder Technol., **58**(1), pp. 63–70.
[20] Lin, Y., McHugh, K. M., Zhou, Y., and Lavernia, E. J., 2007, "Modeling the Spray Forming of H13 Steel Tooling," Metall. Mater. Trans. A, **38**(7), pp. 1632–1637.
[21] He, X., Yu, G., and Mazumder, J., 2010, "Temperature and Composition Profile During Double-Track Laser Cladding of H13 Tool Steel," J. Phys. D: Appl. Phys., **43**(1), p. 015502.
[22] Bergström, D., Kaplan, A., and Powell, J., 2003, "Mathematical Modelling of Laser Absorption Mechanisms in Metals: A Review," 16th Meeting on Mathematical Modelling of Materials Processing with Lasers, Igls, Austria, Jan. 20–24, pp. 19–48.
[23] Putman Publishing Company and OMEGA Press, 1998, "Emissivities of Common Materials," *Transactions in Measurement and Control*, Putman Publishing Company and OMEGA Press LLC, Schaumburg, IL, pp. 72–76.
[24] He, X., Fuerschbach, P., and DebRoy, T., 2003, "Heat Transfer and Fluid Flow During Laser Spot Welding of 304 Stainless Steel," J. Phys. D: Appl. Phys., **36**(12), p. 1388.
[25] Zhu, G., Li, D., Zhang, A., Pi, G., and Tang, Y., 2011, "The Influence of Standoff Variations on the Forming Accuracy in Laser Direct Metal Deposition," Rapid Prototyping J., **17**(2), pp. 98–106.